

# The Collection Efficiency of Shielded and Unshielded Precipitation Gauges. Part I: CFD Airflow Modeling

MATTEO COLLI AND LUCA G. LANZA

*Department of Civil, Chemical and Environmental Engineering, University of Genoa, and WMO-CIMO  
Lead Centre "B.Castelli" on Precipitation Intensity, Genoa, Italy*

ROY RASMUSSEN

*National Center for Atmospheric Research, Boulder, Colorado*

JULIE M. THÉRIAULT

*Department of Earth and Atmospheric Sciences, University of Quebec at Montreal, Montreal, Quebec, Canada*

(Manuscript received 16 January 2015, in final form 18 June 2015)

## ABSTRACT

The aerodynamic response of snow gauges when exposed to the wind is responsible for a significant reduction of their collection performance. The modifications induced by the gauge and the windshield onto the space–time patterns of the undisturbed airflow deviate the snowflake trajectories. In Part I, the disturbed air velocity field in the vicinity of shielded and unshielded gauge configurations is investigated. In Part II, the airflow is the basis for a particle tracking model of snowflake trajectories to estimate the collection efficiency. A Geonor T-200B gauge inside a single Alter shield is simulated for wind speeds varying from 1 to 8 m s<sup>-1</sup>. Both time-averaged and time-dependent computational fluid dynamics simulations are performed, based on Reynolds-averaged Navier–Stokes (RANS) and large-eddy simulation (LES) models, respectively. A shear stress tensor  $k$ – $\Omega$  model (where  $k$  is the turbulent kinetic energy and  $\Omega$  is the turbulent specific dissipation rate) is used for the RANS formulation and solved within a finite-volume method. The LES is implemented with a Smagorinsky subgrid-scale method that models the subgrid stresses as a gradient-diffusion process. The RANS simulations confirm the attenuation of the airflow velocity above the gauge when using a single Alter shield, but the generated turbulence above the orifice rim is underestimated. The intensity and spatial extension of the LES-resolved turbulent region show a dependency on the wind speed that was not detected by the RANS. The time-dependent analysis showed the propagation of turbulent structures and the impact on the turbulent kinetic energy above the gauge collecting section.

## 1. Introduction

In situ measurements of liquid and solid precipitation at the ground use catching and noncatching gauges. Catching-type gauges collect the precipitation into a measuring bucket, where it is quantified using various technologies. Noncatching-type gauges detect precipitation particles using optical or other remote means (using reflectivity, optical beams, vibrations, etc.) when crossing through a sample

volume or impacting a surface, with no need to collect water.

Catching-type instruments are routinely adopted by national weather services for operational use and may provide a high level of measurement accuracy when proper adjustment and correction techniques are applied (Duchon 2008; Lanza and Stagi 2008; Colli et al. 2013a). Noncatching-type gauges are mostly used in research studies or within instrument testing or intercomparison campaigns (Lanza and Stagi 2009; Rasmussen et al. 2012). Quantifying the accuracy of liquid and solid precipitation measurements requires separation of the instrumental sources of uncertainty from influences due to environmental conditions. Instrumental errors relate to the individual sensor design

---

*Corresponding author address:* Matteo Colli, Department of Civil, Chemical and Environmental Engineering, University of Genoa, Via Montallegro 1, CAP 16145 Genoa, Italy.  
E-mail: matteo.colli@unige.it

and their nature is often systematic, allowing for the application of correction algorithms based on laboratory calibration tests. The counting performance of catching-type gauges (i.e., their capability of correctly quantifying the amount of precipitation once collected into the bucket) is generally affected by instrumental errors.

Environmental factors can impact the measurement accuracy as well, depending on the atmospheric conditions at the collector, the siting characteristics (WMO 2008), and other factors. Most of them affect the catching performance of the instrument (i.e., its capability to collect the precise amount of precipitation that would ultimately reach the surface of the ground over the associated footprint area). Typical environmental factors are the gradients of atmospheric temperature, wind speed, and solar radiation. Environmental factors typically result in significant underestimation of cumulated precipitation as documented in the literature (Sevruk 1982; Legates and Willmott 1990; Yang et al. 1999; Rasmussen et al. 2012).

Among the catching-type technologies, the weighing gauge (WG) is characterized by a gravimetric measuring principle (the bucket is continuously weighed to assess changes of the contained water volume over time). The time-varying characteristics of precipitation, the dynamic response of the gauge (Colli et al. 2013b) noise filtering, and the environmental conditions systematically impact the accuracy of WG measurements.

Wind plays a major role among the environmental factors. An underestimation of precipitation by catching-type gauges due to the wind speed has been observed (the so-called exposure problem) and documented (Jevons 1861; Robinson and Rodda 1969; Sevruk et al. 1991). This notwithstanding, a comprehensive understanding of the systematic bias due to the wind has not been achieved, and the assessment of the associated undercatch has been recognized as a central objective of the current Solid Precipitation Intercomparison Experiment (SPICE) of the WMO (Nitu et al. 2012).

The exposure problem is due to the aerodynamic characteristics of the gauge geometry (Folland 1988). The presence of the gauge body modifies the airflow pattern near the collector with respect to the undisturbed configuration. This effect can be easily visualized in a wind tunnel experiment by using smoke trails [after Rasmussen et al. (2012)]. Nešpor and Sevruk (1999) carried out wind tunnel experiments and monitored the air velocity field above the gauge orifice by using a tungsten wire sensor at high sampling frequency. They show (see their Fig. 4) time-averaged contour plots of the magnitude of velocity vector and turbulent kinetic energy. A separation layer is evident between the flow

recirculating within the gauge collector and the external main flow patterns above the orifice. Strangeways (2004) also reports on this effect in the field by providing a visualization based on high-frequency video recording of a light nylon thread tracer, held fixed upstream of the gauge. The final report of the WMO Solid Precipitation Measurement Intercomparison (SPMI; Goodison et al. 1998) contains details of the aerodynamic response of different orifice shapes and dimensions.

Because of the flow distortion, hydrometeor trajectories are deflected when approaching the gauge and tend to follow the local airflow streamlines pattern, partially bypassing the surface area of the collector, with a resulting undercatch of precipitation. The impact of wind-induced losses increases with the horizontal wind speed and depends on the gauge shape, the use of windshields, and the type of precipitation (Smith 2009; Thériault et al. 2012). In operational measurements, various types of windshield configurations are adopted as a solution to limit the exposure problem. The Double Fence Intercomparison Reference (DFIR) shield has been introduced as part of the international reference gauge during the third WMO SPMI (Goodison et al. 1998). Golubev and Simonenko (1992) studied the performance of three different versions of a double-fence shield at the Valdai experimental site (Russia) by using a bush gauge as the primary field reference. The Valdai experiment was continued over the years (Yang et al. 1999; Yang 2014), allowing the revision of the DFIR collection efficiency estimates. The DFIR also includes an inner and smaller metal shield initially constituted by the Tretyakov fence (Goodison et al. 1998), more recently replaced by a single Alter (SA) shield (Rasmussen et al. 2001, 2012). Manual and automated snow gauges installed within modern DFIR shields constitute the primary and the secondary field reference for the WMO SPICE, respectively.

The single Alter shield, originally proposed by J. Cecil Alter (Alter 1937) and eventually modified by the Norwegian Meteorological Institute (Smith et al. 2012), is composed of 32 stainless steel blades (or slats) hinged at a support ring. The upper edge of the blades is positioned slightly above the gauge orifice level. The SA is considerably smaller than the DFIR, and the blades are free to adapt their inclination according to the wind to inhibit snow capping through their motion. The SA shield is commonly adopted by national weather services for snow measurements and is part of the third level reference for SPICE.

The available windshields only mitigate the exposure problem and corrections to the measured values are necessary. Correction methodologies were proposed by various authors: Sevruk (1982) proposed multiplicative correction factors derived from observations with paired

gauges. The empirical analysis is limited to the few measurement sites where reference gauges are present. Furthermore, it does not explain the observed differences between the various possible gauge shapes and height and cannot be extended easily beyond the tested configurations. Transferability of these corrections is doubtful and hard to implement operationally.

In recent years, Nešpor and Sevruk (1999), Constantinescu et al. (2007), Thériault et al. (2012), and Colli (2014) proposed a computational fluid dynamics (CFD) approach to study the wind-induced undercatch. This approach singles out the exposure effects from other sources of error occurring in field experiments. The initial studies either used a simplified fluid dynamics model (Nešpor and Sevruk 1999), with a coarse grid resolution to limit the computational burden, or solved the airflow turbulence without predicting the impact on hydrometeors trajectories (Constantinescu et al. 2007). Recent studies by Thériault et al. (2012) and Colli (2014) showed reasonable agreement between the simulated collection efficiency and field data. This paper (Part I) extends these studies to examine the time-dependent airflow above unshielded and Single Alter shielded gauges. In Colli et al. (2015, hereafter Part II) the airflow is the basis for a particle tracking model of snowflake trajectories to estimate the collection efficiency.

#### a. Infield data analysis

The catch bias due to the exposure problem is measured by the collection efficiency (CE) parameter (Thériault et al. 2012). This is the ratio of the precipitation water equivalent depth  $h_c$  (mm) collected by a gauge exposed to the wind and the depth  $h_a$  (mm) collected by the same gauge in undisturbed conditions (where the gauge is transparent to the wind):

$$CE = \frac{h_c}{h_a}. \quad (1)$$

Existing estimates of the collection efficiency of shielded and unshielded gauges based on field measurements are obtained by assuming as a reference (the true value of precipitation) a collocated DFIR system (Goodison et al. 1998; Rasmussen et al. 2012; Thériault et al. 2012). The final report of SPMI (Goodison et al. 1998) indicates that a significant influence of the horizontal wind speed on the DFIR measurements is detectable, based on a comparison conducted at the Val dai field site where the primary reference is the Tretyakov gauge shielded by a field of shrubs that were trimmed to the level of the gauge orifice.

Thériault et al. (2012) provided an assessment of the collection efficiency of a Geonor T-200B vibrating wire

gauge installed in a single Alter windshield at the Marshall field test site, Colorado (Rasmussen et al. 2012). Vibrating wire gauges are weighing gauges where the bucket is hung on a number of metal wires whose frequency of vibration is measured to derive the weight of the collected precipitation. Average measurements at 10-min intervals were provided for the winter of 2009/10 (December–March). The reported median value of CE is larger than 0.9 at wind speeds  $U_w$  lower than  $2 \text{ m s}^{-1}$ , while at  $U_w \geq 7 \text{ m s}^{-1}$  the collection efficiency is nearly constant at  $CE \approx 0.2$ . Using a visual analysis of the hydrometeors, the authors demonstrated that the scatter of the CE values observed in the  $2 \leq U_w \leq 8 \text{ m s}^{-1}$  range was in large part related to the variability of snow crystal types and associated terminal velocity. Similar experimental comparisons between collocated Geonor T-200B gauges within either the DFIR or the SA shields are currently ongoing in SPICE at different field sites. The Haukelisetter field site (Norway) also provides a typical dataset using hourly data (Wolff et al. 2015).

#### b. Existing CFD approaches

The coupling of advanced airflow models with particle trajectory algorithms is a promising methodology to investigate the gauge exposure effect. This approach has become possible because of the increased computation capabilities of modern high-performance computing (HPC) systems. Folland (1988) estimated the catching capabilities of an inverted conical collector with a large semivertical angle by means of a wind tunnel study employing a physical model. The trajectories' simulations were conducted based on air velocity fields extrapolated from hot-wire anemometer measurements made in the wind tunnel environment (Robinson 1968; M. Green and P. Helliwell 1975, unpublished manuscript). A limitation of this approach is the need to deal with likely errors associated with the insertion of a physical probe into the airstream of the wind tunnel. Furthermore, it is not possible to describe the entire domain surrounding the gauge since some regions are inaccessible to the measuring probe.

With the purpose to overcome such restrictions, Nešpor (1995) and Nešpor and Sevruk (1999) performed finite-volume CFD simulations based on the solution of the Reynolds-averaged Navier–Stokes (RANS) model in the two-equation  $k$ – $\varepsilon$  formulation (where  $k$  is the turbulent kinetic energy and  $\varepsilon$  is the turbulent dissipation). This approach allows an Eulerian description of the air velocity components over the three-dimensional spatial domain in time-averaged terms. The computation of the particle trajectories was conducted with a Lagrangian method assuming the raindrop motion did not interfere with the airflow. Another important

simplification was to neglect possible collisions, coalescences, and breakups between the falling particles. This notwithstanding, the possibility to simulate detailed air velocity fields allowed for calculation of the collection efficiency for a wide variety of gauges [Mk2, Hellman, Administration des services techniques de l'agriculture (ASTA), and OTT Pluvio]. Constantinescu et al. (2007) performed further steps toward accurate computation of airflow fields around the gauge shape with the employment of more advanced turbulence simulations. The work shows a detailed comparison between airflows realized around a MetOne rain gauge and computed by RANS and large-eddy simulation (LES) models, obtaining both time-independent and time-dependent solutions. One of the main outcomes of this work is the evidence that the various RANS models ( $k$ - $\varepsilon$  and shear stress tensor  $k$ - $\Omega$ , where  $\Omega$  is the turbulent specific dissipation rate) predicted very similar vorticity distributions, and compared well with the LESs, irrespective of the wind direction. On the other hand, the distribution of the turbulent kinetic energy ( $k$ ) was highly dependent on the RANS model used with strong deviations from the more accurate LES values around critical regions near the collecting area of the gauge. Noting that  $k$  is an index of the magnitude of the velocity fluctuations, high levels of  $k$  impact the particle trajectories through the exchange of momentum between the airflow and the precipitation crystals. The authors found that the LES approach appears to be the best suited to accurately predict the trajectories of the raindrops around the rain gauges because the RANS models cannot capture the dynamics of the eddies and the associated turbulent diffusion and transport phenomena. Colli (2014), who proposed an approximated evaluation of the Stokes time  $\tau_p$  (s), or viscous relaxation time, for snow particles supports these considerations. He showed that the dry snow crystals have limited  $\tau_p$  values, comparable with the periods of the airflow turbulence fluctuations.

A comprehensive investigation of the collection efficiency by means of RANS models was conducted by Thériault et al. (2012) for the SA shielded Geonor T-200B gauge. The airflow dataset was composed of 10 air velocity fields obtained with different undisturbed wind speeds within  $1 \leq U_w \leq 10 \text{ m s}^{-1}$ . In this work, the trajectories of different snow types were simulated with a Lagrangian code for 16 different particle diameters ranging from 0.25 to 20 mm.

A comparison with CE estimates measured at the Marshall field test site was performed, showing that a large part of the observed CE scatter could be ascribed to the variability of the terminal velocity of different ice crystals. The simulated cases of dry and wet snow result

in two extreme CE( $U_w$ ) curves that compare well to the observations.

The present work reports an evaluation of three-dimensional RANS air velocity and turbulent kinetic energy fields computed with a fine spatial discretization in order to describe accurately the airflow patterns realized near the collector walls. Both SA shielded and unshielded gauges are considered in the time-averaged investigation. A dedicated session of LES is carried out for the SA shielded Geonor T-200B configuration to provide time-dependent solutions. In Part II, the improvement due to the use of the SA windshield is demonstrated in terms of the collection efficiency.

## 2. Airflow investigation method

### a. Geometry

The present analysis focuses on a measuring system composed by the Geonor T-200B snow gauge and the SA windshield as used in SPICE.

The Geonor T-200B is an automatic catching-type precipitation gauge exploiting the vibrating wire technology (Bakkehoi et al. 1985), which provides high-sensitivity measurements of the liquid equivalent of atmospheric particles once they enter the collector. The gauge uses three measuring sensors and is available on the market with different sizes of the catching area and bucket capacities. The version adopted in the present analysis has an orifice diameter  $D$  equal to 0.16 m and a maximum water equivalent depth equal to 600 mm (Fig. 1). In usual practice, the gauge orifice should be located at a sufficiently high level above the ground such that the upstream airflow is unaffected by the presence of surrounding obstacles; in this work, an arbitrary height of 1.55 m was considered.

The Geonor T-200B is widely used for both liquid and solid precipitation measurements with a variety of windshielding solutions (Smith 2009). The coupling with an Alter-type shield is typical because of its small size and mounting simplicity. Although the SA is also available in a double-fence version, this study will consider only a single-fence configuration. The SA blades are free to rotate on a horizontal axis along the circular ring connection and the spacing between each element is  $s = 0.04 \text{ m}$ . These two factors play a crucial role in the windshield aerodynamic efficiency since they govern the flux of air penetrating the shield and act as a relevant source of turbulence.

### b. The time-averaged approach

The time-independent simulations developed in this work are based on the RANS equations with a shear

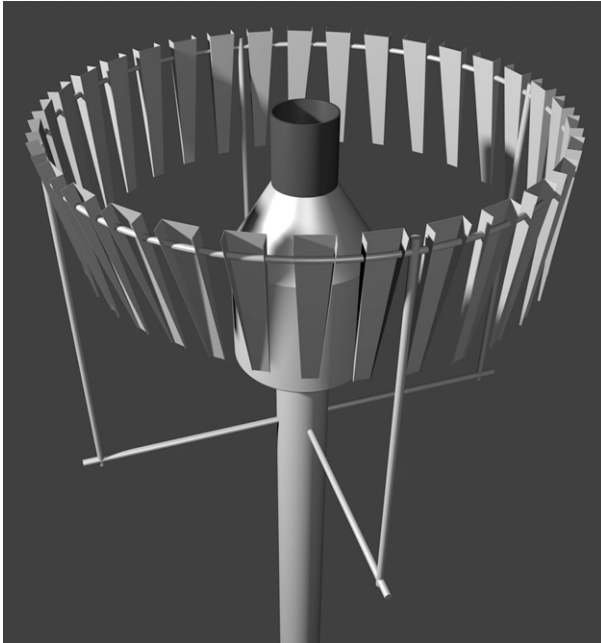


FIG. 1. Model of the geometry of a Geonor T-200B vibrating wire gauge installed within an SA windshield.

stress tensor  $k-\Omega$  model, which is widely used in common CFD practice for a number of turbulence problems (Wilcox 2006). The basic formulation of this model couples the governing equation of the turbulent kinetic energy (i.e.,  $k$ ;  $\text{m}^2 \text{s}^{-2}$ ) with a second transport equation for turbulent specific dissipation rate (i.e.,  $\Omega$ ;  $\text{s}^{-1}$ ). The use of a shear stress tensor version of the standard  $k-\Omega$  formulation makes the model directly usable all the way down to the walls (i.e., the ground and the windshield-gauge surface) through the viscous sublayer where the flow is laminar and the velocity

decrease toward a no-slip condition. The shear stress tensor  $k-\Omega$  model switches to a common  $k-\epsilon$  behavior (see Wilcox 2006) in the free stream and thereby avoids the common  $k-\Omega$  problem of the model being too sensitive to the inlet free-stream turbulence properties.

The three-dimensional air velocity and pressure fields are solved with a finite-volume method implemented using the OpenFOAM CFD package. A set of stationary wind speed cases ranging from  $1$  to  $10 \text{ m s}^{-1}$  (with increments of  $1 \text{ m s}^{-1}$ ) are run for both the shielded and unshielded gauge configurations.

The spatial computational domain consists of an  $8 \text{ m} \times 18 \text{ m} \times 18 \text{ m}$  environmental box with the geometries of the gauge and windshield located in the center of one of the two major bases. The three coordinates are oriented such that the  $z$  axis refers to the vertical, while the  $x$  axis is along the streamwise direction and  $y$  is along the crosswise direction. The origin of the axes lies at the base of the cylindrical gauge stand and specifically in the center of its cross section in order to exploit the axial symmetry of the gauge and windshield bodies.

The three-dimensional spatial domain is described by an unstructured hybrid tetrahedral-prism mesh depending on the geometries and the model to be applied. The prism elements are well suited to bind the bidimensional triangular elements laying on the modeled geometries with some well-staggered layers of cells (as in Fig. 2) that refine the regions affected by high gradients in the transport equations (Marshall and Plassmann 2000; Davis et al. 2012). The oscillating blades are simplified as fixed geometries by imposing an upwind blades angle with respect to the vertical equal to  $15^\circ$  at horizontal wind speed  $1 \leq U_w \leq 5 \text{ m s}^{-1}$  and equal to  $30^\circ$  when  $U_w \geq 6 \text{ m s}^{-1}$  (Thériault et al. 2012).

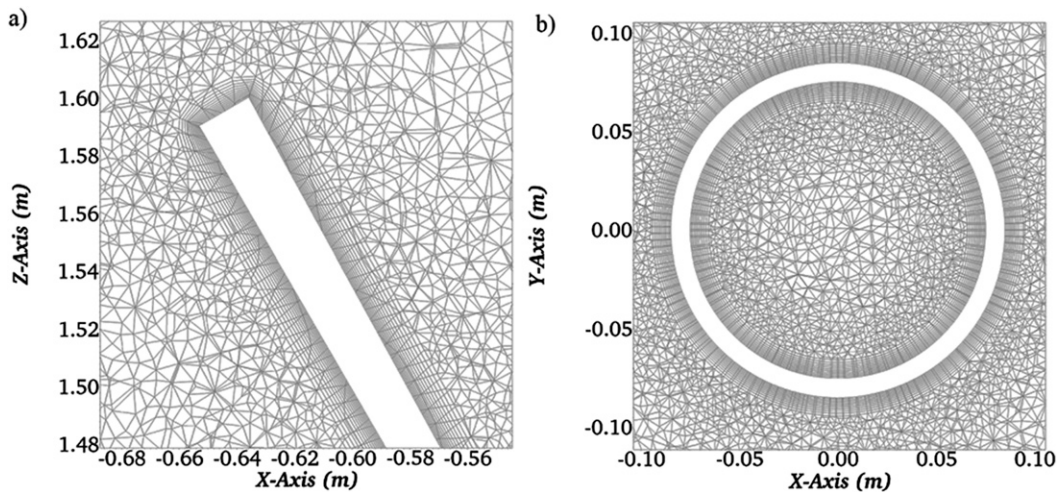


FIG. 2. Mesh refinement layers for the (a) vertical section ( $y = 0 \text{ m}$ ) of an SA shield element and (b) horizontal section ( $z = 1.60 \text{ m}$ ) of the Geonor T-200B orifice rim.

TABLE 1. Geometric characteristics and quality factors of the different grids adopted for the RANS simulation and LES.

Model	No. of elements ( $\times 10^6$ )		Max cell skewness	Max cell nonorthogonality	Max cell aspect ratio
	Tetrahedra	Prisms			
RANS 15°	0.5	1.0	2.7	69.3	291.4
RANS 30°	0.7	1.5	2.9	68.2	94.8
RANS unshielded	1.5	4.7	2.7	67.3	161.3
LES 15°	5.5	22.0	2.7	67.4	84.5
LES 30°	6.1	23.4	2.7	69.8	84.5

The quality of the mesh was verified by using the standard parameters of orthogonality, skewness, and aspect ratio (Jasak 1996). Table 1 reports the number of elements composing the grid and selected quality factors such as the maximum skewness measured in the whole cells sample, the maximum elements nonorthogonality, and the maximum cells aspect ratio. The mesh has prismatic refinement layers composed by 13 cells (counted along the normal direction  $y$  to the wall) whose spacing is governed by a constant growth rate equal to 1.2 with the first node generally located at  $y = 0.5$  mm.

The airflow is solved by modeling the boundary layer regions of the flow (close to the ground and the windshield–snow gauge surfaces) with specific wall functions defined according to the variables solved (the turbulent kinematic viscosity  $\nu_T$ ,  $k$ , and  $\Omega$ ). This is reasonable since the problem of the wind-driven turbulence is dominated by the free flow regions, and the wall function method reduces the computational burden of the simulation. The nondimensional wall unit function is defined as  $y^+ = (yu_T)/\nu_a$ , where  $y$  (m) is the distance to the wall,  $u_T$  ( $\text{m s}^{-1}$ ) is the friction velocity, and  $\nu_a$  ( $\text{m}^2 \text{s}^{-1}$ ) is the kinematic viscosity of the carrying fluid. As a good CFD practice, the  $y^+$  values realized at the first mesh node around the objects' surfaces are checked in postprocessing, this being necessary since the values of the friction velocity are not known a priori. The mesh has been therefore adjusted in order to dimensionalize the first cell layer within  $30 < y^+ < 200$  and to apply a Spalding wall function for modeling the airflow boundary layer (Spalding 1961). The Spalding methodology proposes a single formula that is valid over the whole range of dimensionless distance to describe the universal turbulent velocity profile. The main advantages of modeling the near-wall region instead of integrating the governing equations is the lower number of grid points required by the solver to run successfully with a general reduction of computation time. This may also avoid high aspect ratio cells, with a subsequent improvement of the mesh quality and the associated numerical benefits.

The fluid “air” has been characterized as a Newtonian incompressible fluid with a kinematic viscosity  $\nu_a = 1.2 \times 10^{-5} \text{ m}^2 \text{ s}^{-1}$  and an air density  $\rho_a = 1.3 \text{ kg m}^{-3}$ , consistent

with an air temperature  $T_a = 0^\circ\text{C}$ . In the present work, we neglect the increase in air density at lower temperatures.

### c. The time-dependent approach

Time-dependent airflows are computed by means of an LES model. The basic idea behind the LES approach is that one can explicitly solve for the large eddies in the calculation and implicitly account for the small eddies that are energetically weaker. The assumption is that the small eddies provide a limited contribution to the Reynolds stresses and are nearly isotropic with universal characteristics (irrespective of the geometry). The implicit solution of these scales is carried out by using a subgrid-scale model (Wilcox 2006). Practically, the velocity field is separated into a resolved (representing the large eddies) and a subgrid part responsible for the small eddies whose effect on the resolved field is included through the subgrid-scale model. In the literature, the separation of the velocity field into a resolved and a filtered scale is referred to as a filtering operation, which in this work is implicit in the spatial grid itself (a methodology that is also called box filter). Table 1 shows the number of elements and the quality parameters of the three-dimensional mesh adopted to run the LES model. A large amount of tetrahedral and prism elements was necessary to solve for small turbulence scales that do not meet the condition of near-isotropy and weak energy content and would be filtered out by a coarser mesh. As for section 2b, we use prism finite volumes to refine the boundary layers around the gauge and the windshield walls. The thickness of the first cell layer around the walls was again designed to fall in the inertial sublayer ( $y^+ \approx 30\text{--}200$ ) to model the transition of the velocity profile and the associated shear stresses with the Spalding formula for the law of the wall (Spalding 1961).

The simulations performed in this work implement a Smagorinsky subgrid-scale (SGS) method, which models the subgrid stress as a gradient-diffusion process, assuming an analogy with a molecular motion (Wilcox 2006). The eddy viscosity  $\nu_T$  is given by

$$\nu_T = (C_s \Delta)^2 \sqrt{S_{ij} S_{ij}}, \quad (2)$$

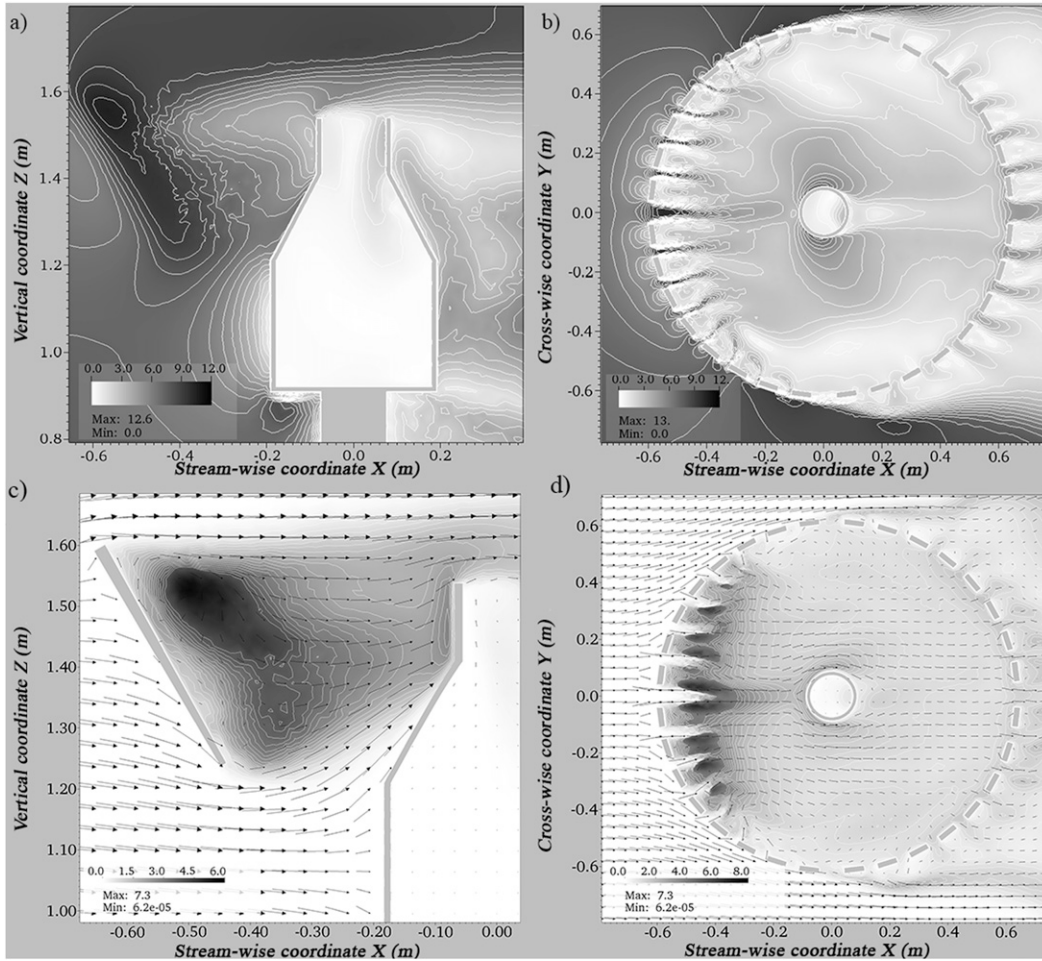


FIG. 3. Magnitude of velocity (i.e.,  $U$ ; m s<sup>-1</sup>) contours on a (a) vertical and (b) horizontal section and turbulent kinetic energy (i.e.,  $k$ ; m<sup>2</sup> s<sup>-2</sup>) contours and velocity vectors on a (c) vertical and (d) horizontal section computed by the RANS  $k$ - $\Omega$  shear stress tensor model with  $U_w = 8$  m s<sup>-1</sup>.

where  $C_S$  is the Smagorinsky coefficient (equal to 0.167),  $\Delta = V^{(1/3)}$  is the size of the grid computed at any location of the bounding box,  $V$  is the cell volume, and  $S_{ij}$  is the strain rate tensor defined as

$$S_{ij} = \frac{1}{2} \left( \frac{\partial \bar{u}_i}{\partial x_j} + \frac{\partial \bar{u}_j}{\partial x_i} \right). \quad (3)$$

A constant air velocity profile along the vertical and crosswise directions has been assumed on the bounding box inlet. Therefore, effects due to the turbulence in the incoming airflow and the height of the collector with respect to a rough ground are neglected and are the subject of future work. Because of the adoption of the law of the wall in the near-wall regions, no special treatment of Eq. (3) is required to adjust empirically the SGS method at the solid surfaces (e.g., inclusion of damping terms).

The initialization of the solution was performed by mapping the turbulent kinetic energy and air velocity time-averaged values computed by the RANS model onto the LES spatial mesh. This allowed faster convergence of the large-eddy simulations.

### 3. Air velocity fields

#### a. RANS airflows

The airflow pattern around a Geonor T-200B snow gauge in an SA shield configuration is presented in this section. The undisturbed airflows are perpendicular to the spacing between two upwind blades. Figures 3a and 3b show the spatial distribution of the magnitude of the velocity  $U$  obtained by the shear stress tensor  $k$ - $\Omega$  RANS model at  $U_w = 8$  m s<sup>-1</sup>.

Figure 3a represents the magnitude of velocity contour plots interpolated on a vertical streamwise direction ( $y = 0$ )

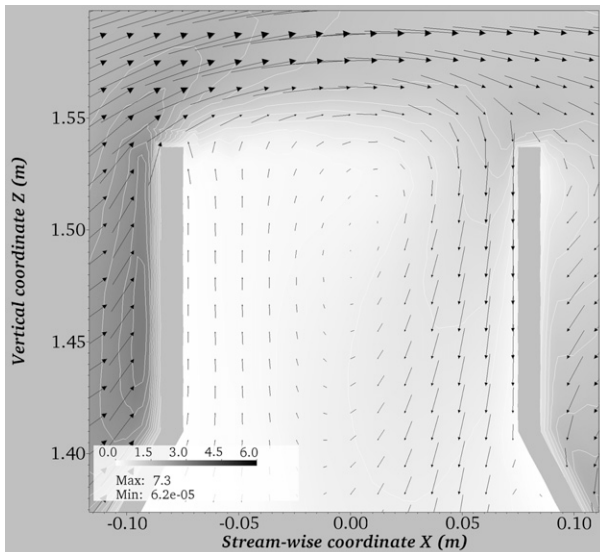


FIG. 4. Airflow velocity vectors and turbulent kinetic energy (i.e.,  $k$ ;  $\text{m}^2 \text{s}^{-2}$ ) contours on a streamwise vertical plane (located at  $y = 0$  m) computed by the RANS  $k$ - $\Omega$  shear stress tensor model with  $U_w = 8 \text{ m s}^{-1}$ . A close view of the gauge orifice is shown. The length of the vectors is proportional to the velocity magnitude computed in correspondence on the arrows tip.

that cuts the Geonor T-200B shape in half, showing the values obtained inside the simplified gauge geometry. The continuity of the air mass flowing through the spatial domain obstructed by the SA shield causes an increasing velocity within the spacing between the upwind blades. This effect is immediately balanced in the region downstream of the blades (the blades shadow) that is characterized by very low or negative longitudinal velocity components generally resulting in a reduced wind speed zone, with  $U < U_w$ , just around the gauge orifice. Figure 3a also shows that the velocity magnitude increases with increasing vertical distance above the gauge orifice to higher values than  $U_w$ .

In Fig. 3b, the horizontal plane located at the snow gauge collector level shows that the orifice is separated into a dark and a lighter zone, demarcating an updraft and a downdraft zone. This is also visible in Fig. 4, where the gauge collector is crossed by airflow vectors that are directed upward close to the upstream wall of the orifice and downward close to the downstream wall. The difference between the two regions becomes stronger at higher undisturbed wind speeds. This effect can have a direct impact on the particle trajectories, facilitating the catching in the downdraft section and forcing out the trajectories in the updraft zone. The continuity of the air mass contained within the gauge walls must be respected since they form a closed geometry; hence, the internal domain represents a recirculation zone (Nešpor and Sevruc 1999).

It is worth stressing that the consequence of simulating a wind direction that is perpendicular to the blade spacing (rather than to a blade face) results in higher streamwise velocity components just upwind of the gauge orifice. Further study on the impact of different windshield orientations is recommended in order to quantify the airflow sensitivity to the horizontal wind direction.

It is worth noting that the shoulders of the Geonor T-200B body foster the generation of a significant updraft along the outer upwind side of the gauge. These fluxes drift up the nearly horizontal airflow that approaches the orifice. Such behavior is clearly visible in Figs. 3c and 3d ( $U_w = 8 \text{ m s}^{-1}$ ). Folland (1988) and Nešpor and Sevruc (1999) were the first to report this behavior, and an improved aerodynamic response of different gauge shapes was numerically observed.

The kinetic energy field computed for the  $U_w = 8 \text{ m s}^{-1}$  case, illustrated in Fig. 4, also indicates some vortex production just past the upwind orifice edges with a high vorticity zone coincident with the separation line between the recirculation and the external flow. In the region that surrounds the gauge orifice, a strong deformation of the precipitation trajectories is expected. This results in considerable turbulence production, as shown in the contour plots of Fig. 3 (spatial distribution of the turbulent kinetic energy). Furthermore, the extended high  $k$  zone revealed just above the collecting section is also caused by an additional, but not secondary, source of turbulence represented by the SA blades. The same elements were devised originally to improve the airflow conditions in the proximity of the gauge orifice.

In nondimensional terms we use the vertical coordinate  $z^*/D$  [where  $z^*$  (m) is the distance from the collecting area of the gauge and  $D$  is the collector diameter] and the ratio  $U/U_w$  between the velocity magnitude and the undisturbed wind speed. The turbulent kinetic energy is compared with the squared wind velocity yielding  $k/U_w^2$ . Figures 5a and 5b summarize the results of the RANS model by comparing nondimensional vertical profiles of velocity and turbulent kinetic energy above the gauge at all simulated wind regimes. Figure 5a highlights a quasi-stagnant air region at  $z^* \leq 0.1D$  while at  $z^* = D$  the velocity reaches approximately  $U/U_w = 1.1$  and then asymptotically converges to  $U/U_w = 1.0$  with increasing distance above the orifice level. The  $U/U_w$  curves lay very close to each other, denoting a good repeatability of the time-averaged air velocity profiles above the gauge with varying wind speed. On the other hand, the nondimensional  $k$  graph presents a slightly different behavior between the  $U_w \leq 5 \text{ m s}^{-1}$  and the  $U_w > 5 \text{ m s}^{-1}$  conditions. Figure 5b shows that at  $0.25D < z^* < 0.70D$  and  $U_w > 5 \text{ m s}^{-1}$  the

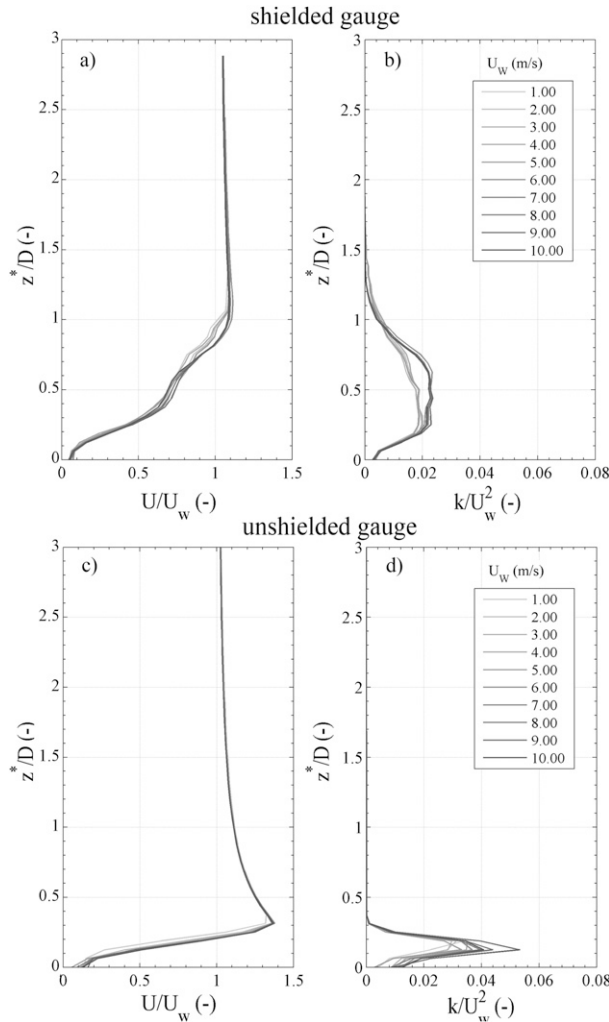


FIG. 5. Time-averaged vertical profile of the normalized magnitude of the (a),(c) air velocity  $U/U_w$  (unitless) and (b),(d) turbulent kinetic energy  $k/U_w^2$  (unitless) computed above an SA shielded (top) and unshielded (bottom) Geonor T-200B orifice level by the RANS  $k-\Omega$  shear stress tensor model.

turbulent kinetic energy exceeds the  $0.02U_w^2$  threshold, maintaining the same nondimensional profile. At lower wind speeds,  $k \leq 0.02U_w^2$  and the shape of the curves is notably different. The reason for such separation of the turbulent behavior around  $U_w = 5 \text{ m s}^{-1}$  is due to the different static windshield geometries modeled in the simulations. As anticipated, this work neglects the oscillating motion of the blades around the mean inclination due to the wind gusts. In the present model, the inclination of the upwind blades abruptly varies from  $15^\circ$  to  $30^\circ$  at  $U_w = 5 \text{ m s}^{-1}$ . The real trend of the  $k/U_w^2$  curves could possibly follow a gradual transition from the lighter group of curves to the darker ones.

The effects of turbulence propagation from the windshield to the critical regions are clear when analyzing the

results of the RANS simulation executed on the unshielded gauge. Figures 5c and 5d adopt the same representation used in Figs. 5a and 5b, allowing a direct comparison between the two datasets. Figure 5c confirms the good performance of the SA windshield in reducing the air velocity above the gauge. If the shielded velocity profile reaches  $1.1U_w$  at  $z^* = 1.1D$ , the unshielded configuration shows a velocity peak equal to  $1.4U_w$  already at  $z^* = 0.3D$ . Above that level, the time-averaged  $U$  slowly converges to  $U_w$ . The normalized velocity curves appear highly repeatable with various horizontal wind speeds. The turbulent kinetic energy observed above the unshielded gauge (Fig. 5d) shows peak values that are twice those observed in the shielded case. However, their spatial distribution has been constricted in a very thin vertical band ( $z^* < 0.3D$ ) that is about 4 times narrower than the turbulent street observed with the shielded gauge. The high sensitivity of the airflow above the collector to the windshield is an additional motivation to analyze accurately the induced turbulence around the gauge by adopting advanced fluid dynamics tools such as the LES modeling.

*b. LES airflows*

The time-dependent flow field resulting from the LES is diagnosed with various airflow velocity and pressure fields saved at a fixed time interval  $dt = 0.05 \text{ s}$ . After having reached numerical convergence, the duration of each run has been limited to the time required by a passive scalar to cross the SA shield diameter three times. This was necessary to cope with the high computational requirements needed to compute time-dependent solutions. In accordance with the proposed criterion, the duration of the  $U_w = 1 \text{ m s}^{-1}$  experiment has been limited to 3.75 s; meanwhile the stronger wind speed case simulated with the LES model ( $U_w = 8 \text{ m s}^{-1}$ ) covered a time span equal to 0.45 s. Figure 6 provides examples of the evolution of  $U$  near the shielded gauge on a streamwise vertical and horizontal plane (defined by their normal coordinates  $y^* = 0.00$  and  $z^* = 0.00$ , respectively). Even if the  $U$  contour plots do not exactly identify the spatial extension of the vortexes, a clear propagation of turbulent fluctuations generated by the upwind windshield elements toward the gauge is apparent as well as the eddy detachment in the wake of the gauge shape.

Recalling that the vertical contour plots of Fig. 6 (top) cuts the free space between the two upwind blades, it is worth remarking that a dark gray zone (high air velocity components) is observed near the windshield and is immediately followed by scattered low-velocity zones. Residual  $U/U_w > 1$  values are observed along the streamwise direction at higher levels than the blades and the gauge upper edges, delimiting a region that is slightly

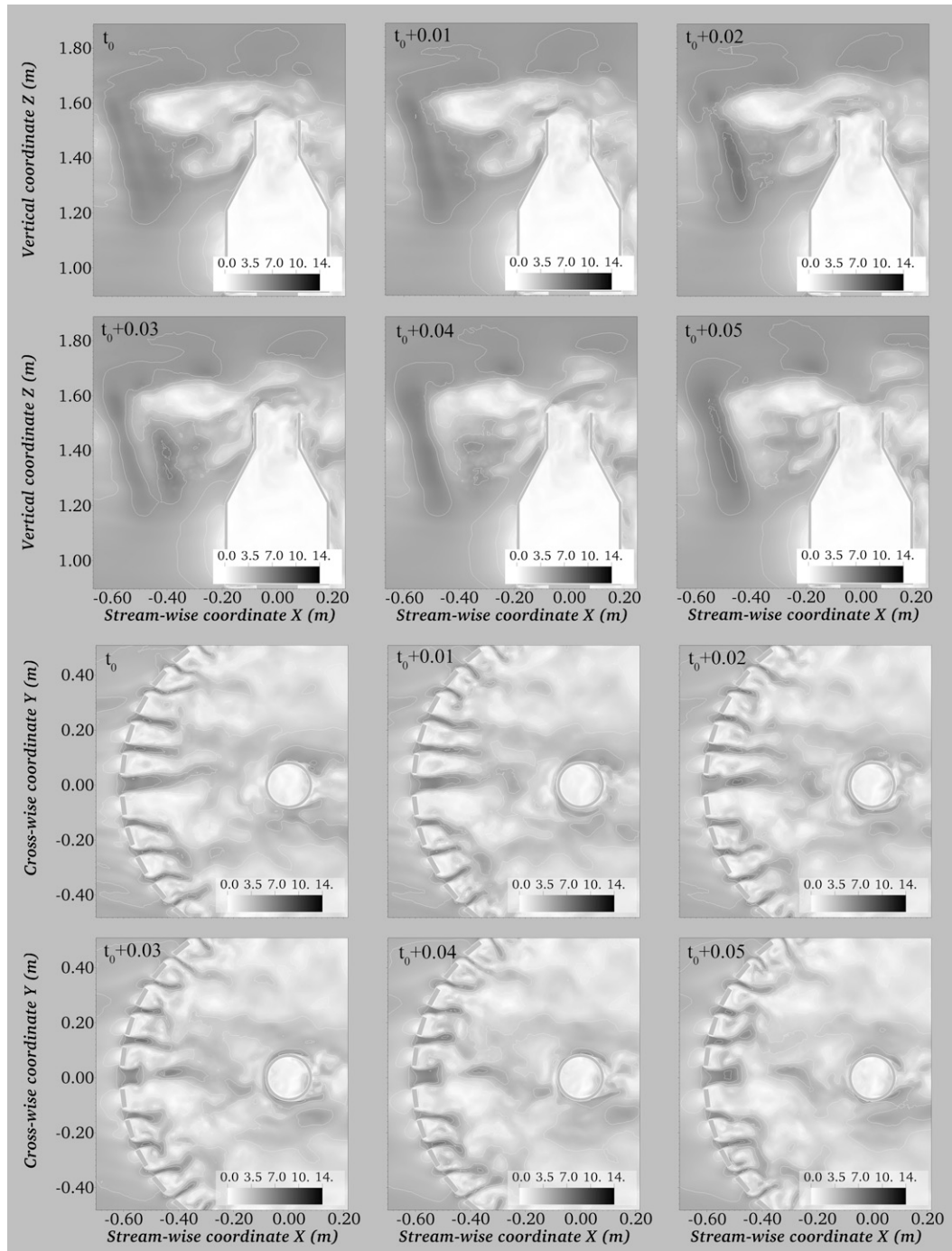


FIG. 6. Sequence of time-dependent magnitude of velocity (i.e.,  $U$ ;  $\text{m s}^{-1}$ ) color plots on a streamwise vertical plane ( $y = 0 \text{ m}$ ) and a horizontal plane located at the orifice level with  $U_w = 5 \text{ m s}^{-1}$ . Frame rate is equal to 0.01 s.

affected by the aerodynamic response of the shield. Anyway, the wide  $U \ll 5 \text{ m s}^{-1}$  regions surrounding the gauge (Fig. 6) demonstrate the shield efficiency in reducing the time-averaged air velocity components, although a strong space–time nonuniformity is observed as well. By comparing one instantaneous panel of Fig. 6

with the steady RANS solution shown in Fig. 3, a significant simplification of the real dynamic behavior of the airflow operated by the RANS time averaging with respect to the LES case is apparent.

In Fig. 7 (top), the actual distribution of the horizontal component of the air velocity  $u/U_w$  at various levels

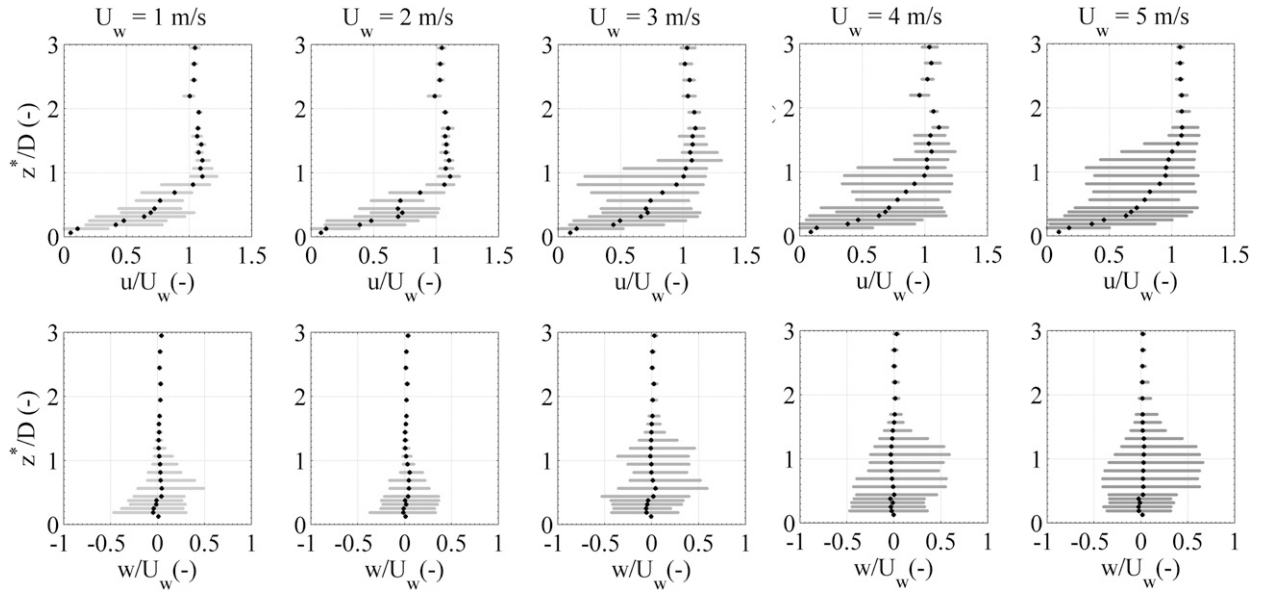


FIG. 7. Vertical profiles of the normalized horizontal  $u/U_w$  (unitless) and vertical  $w/U_w$  (unitless) components of the air velocity above the orifice level ( $z^*/D = 0$ ) of an SA shielded Geonor T-200B computed by the time-dependent LES model.

above the gauge with  $1 \leq U_w \leq 5 \text{ m s}^{-1}$  is depicted in nondimensional terms. While the time-averaged horizontal velocity profile quickly converges to the undisturbed configuration within  $z^* < D$ , the sample distribution maintains a strong variability up to  $z^* = 1.8D$  (see, e.g., the  $U_w = 5 \text{ m s}^{-1}$  case). The  $u/U_w$  scatterplots show a larger asymmetry of the sample distribution when increasing the undisturbed wind speed. A similar representation is also provided for the nondimensional vertical air velocity component  $w/U_w$  in Fig. 7 (bottom), showing low time-averaged values along the vertical axis but nonnegligible fluctuations that increase with  $U_w$ . The evidence that both the normalized  $u/U_w$  and  $w/U_w$  velocity distributions become wider with increasing  $U_w$  suggests a nonlinear behavior of the turbulent fluctuations amplitude, and hence the turbulent kinetic energy, with the surrounding wind regime.

It is convenient to compute and superimpose the nondimensional time-averaged magnitude of velocity  $U/U_w$  and turbulent kinetic energy  $k/U_w^2$  vertical profiles (Fig. 8) with the aim to detect recurrent aerodynamic trends and compare it to the RANS results (Fig. 5). When  $U_w \leq 5 \text{ m s}^{-1}$  the overall behavior of the LES turbulent kinetic energy profiles is less repeatable than what is observed in the shielded RANS simulation. That is, the  $k/U_w^2$  curves show a different form of dependence to the undisturbed wind speed. While the RANS case (Fig. 5b) reveals a turbulent band, which is confined below  $z^* < 1.5D$ , the LES  $k$  profile assumes significant values within  $z^* < D$  with  $U_w = 1 \text{ m s}^{-1}$  and increases its influence zone with  $U_w$  up to  $z^* < 2D$  when the wind

speed is equal to  $5 \text{ m s}^{-1}$  (Fig. 8). Another important difference with respect to the RANS results is represented by the peak values of the  $k$  curves. The  $k$  peak observed with  $U_w = 1 \text{ m s}^{-1}$  is now equal to  $0.03U_w^2 \text{ m}^2 \text{ s}^{-2}$ , and the  $U_w = 5 \text{ m s}^{-1}$  case results in  $k = 0.05U_w^2 \text{ m}^2 \text{ s}^{-2}$  compared with a RANS peak of about  $k = 0.02U_w^2 \text{ m}^2 \text{ s}^{-2}$ . This indicates a general underestimation of the airflow turbulent content in the shear stress tensor  $k$ - $\Omega$  RANS experiments. On the other hand, the time-averaged magnitude of velocity

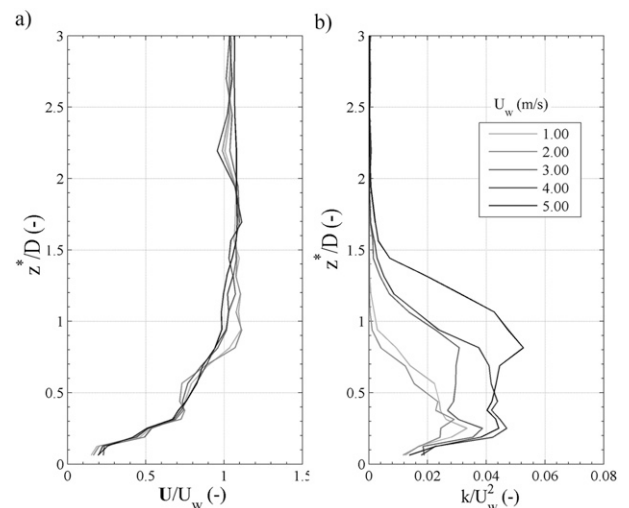


FIG. 8. Time-averaged vertical profile of the normalized magnitude of the (a) air velocity  $U/U_w$  (unitless) and (b) turbulent kinetic energy  $k/U_w^2$  (unitless) computed above the orifice level by the LES model for an SA shielded case.

profiles computed with the LES model provides consistent information with respect to the RANS analysis, confirming the reliability of the shear stress tensor  $k$ - $\Omega$  model when steady-state velocity fields have to be assessed.

#### 4. Conclusions

The numerical evaluation of the airflow pattern realized in the proximity of a typical precipitation gauge under various wind regimes has been performed within a computational fluid dynamics (CFD) approach. Both the unshielded and the single Alter (SA) shielded gauges were shown to significantly impact the time-dependent and time-independent airflow above the shield-gauge system.

The analysis was carried out by performing CFD simulations of the airflow around the Geonor T-200B gauge using both time-invariant and time-variant approaches, based on the Reynolds-averaged Navier–Stokes (RANS) equations and the large-eddy simulation (LES) model. The two models have been run for wind speeds varying from 1 to  $8\text{ m s}^{-1}$ .

A comparison between the RANS- and LES-modeled airflows highlighted a general underestimation of the turbulence by the former model just above the gauge orifice rim. The LES revealed that the intensity and the spatial extension of such a turbulent region show a sort of dependency to the wind speed that was not detected by using a RANS approach. If the shear stress tensor  $k$ - $\Omega$  RANS model generally provides better estimates of the turbulent kinetic energy  $k$  fields than other RANS methods in the regions that are close to the windshield-snow gauge surfaces, the LES reduced the amount of empiricism on the results by directly solving the most energetic eddies.

The RANS simulation showed that the wind speed above the gauge is lower when using an SA shield. Higher values of  $U$  and  $k$  occur above the collector in an unshielded configuration when compared to the SA shield. The study therefore confirms the general benefit of installing an SA shield around the gauge with an expected consequential improvement of the gauge collection performance as observed in field measurements. Despite the overall positive contribution of the windshield in time-averaged terms, the time-variant analysis clearly showed that the propagation of turbulent structures, produced by the aerodynamic response of the SA, has a relevant impact on the mentioned turbulent kinetic energy realized above the gauge collecting section.

An experimental activity on a wind tunnel environment is recommended to validate the different airflow features here predicted by the LES model and the

various assumptions made to keep the computation requirements affordable.

**Part II** takes advantage of the RANS and LES air velocity fields to estimate the wind-induced undercatch of the tested shielded gauge by calculating particle trajectories with a Lagrangian tracking model.

*Acknowledgments.* This research was supported through funding from the Ligurian District of Marine Technology and SITEP Italia (Italy), the National Center for Atmospheric Research (United States) NSF-funded Water System program, and the Natural Sciences and Engineering Research Council (NSERC) of Canada. Field data have been provided courtesy of Dr. Mareile Wolff and the Norwegian Meteorological Institute (<http://met.no/English/>).

#### REFERENCES

- Alter, J., 1937: Shielded storage precipitation gages. *Mon. Wea. Rev.*, **65**, 262–265, doi:10.1175/1520-0493(1937)65<262:SSPG>2.0.CO;2.
- Bakkehoi, S., K. Oien, and E. J. Forland, 1985: An automatic precipitation gauge based on vibrating-wire strain gauges. *Nord. Hydrol.*, **16**, 193–202.
- Colli, M., 2014: Assessing the accuracy of precipitation gauges: A CFD approach to model wind induced errors. Ph.D. thesis, School in Science and Technology for Engineering, University of Genova, 209 pp.
- , L. Lanza, and P. Chan, 2013a: Co-located tipping-bucket and optical drop counter RI measurements and a simulated correction algorithm. *Atmos. Res.*, **119**, 3–12, doi:10.1016/j.atmosres.2011.07.018.
- , —, and P. La Barbera, 2013b: Performance of a weighing rain gauge under laboratory simulated time-varying reference rainfall rates. *Atmos. Res.*, **131**, 3–12, doi:10.1016/j.atmosres.2013.04.006.
- , —, R. Rasmussen, and J. M. Thériault, 2015: The collection efficiency of shielded and unshielded precipitation gauges. Part II: Modeling particle trajectories. *J. Hydrometeorol.*, **17**, 245–255, doi:10.1175/JHM-D-15-0011.1.
- Constantinescu, S., W. Krajewski, C. Ozdemir, and T. Tokyay, 2007: Simulation of flow around rain gauges: Comparison of LES with RANS models. *Adv. Water Resour.*, **30**, 43–58, doi:10.1016/j.advwatres.2006.02.011.
- Davis, P., A. Rinehimer, and M. Uddin, 2012: A comparison of RANS-based turbulence modeling for flow over a wall-mounted square cylinder. CD-Adapco Tech. Memo., 8 pp.
- Duchon, C., 2008: Using vibrating-wire technology for precipitation measurements. *Precipitation: Advances in Measurement, Estimation and Prediction*, S. Michaelides, Ed., Springer, 33–58, doi:10.1007/978-3-540-77655-0\_2.
- Folland, C., 1988: Numerical models of the raingauge exposure problem, field experiments and an improved collector design. *Quart. J. Roy. Meteor. Soc.*, **114**, 1485–1516, doi:10.1002/qj.49711448407.
- Golubev, V., and A. Yu. Simonenko, 1992: Results of comparison of network methods of precipitation observation in winter. *Soviet Meteor. Hydrol.*, **5**, 80–86.

- Goodison, B., P. Louie, and D. Yang, 1998: WMO solid precipitation intercomparison. Instruments and Observing Methods Rep. 67, WMO/TD 872, 212 pp. [Available online at <https://www.wmo.int/pages/prog/www/IMOP/publications/IOM-67-solid-precip/WMOtd872.pdf>.]
- Jasak, H., 1996: Error analysis and estimation for the finite volume method with applications to fluid flows. Ph.D. thesis, Department of Mechanical Engineering, Imperial College of Science, Technology and Medicine, University of London, 394 pp.
- Jevons, W., 1861: On the deficiency of rain in an elevated rain-gauge, as caused by wind. *London, Edinburgh Dublin Philos. Mag. J. Sci.*, **22**, 421–433. [Available online at <http://www.tandfonline.com/doi/abs/10.1080/14786446108643180>.]
- Lanza, L., and L. Stagi, 2008: Certified accuracy of rainfall data as a standard requirement in scientific investigations. *Adv. Geosci.*, **16**, 43–48, doi:10.5194/adgeo-16-43-2008.
- , and —, 2009: High resolution performance of catching type rain gauges from the laboratory phase of the WMO Field Intercomparison of Rain Intensity Gauges. *Atmos. Res.*, **94**, 555–563, doi:10.1016/j.atmosres.2009.04.012.
- Legates, D., and C. Willmott, 1990: Mean seasonal and spatial variability in gauge-corrected, global precipitation. *Int. J. Climatol.*, **10**, 111–127, doi:10.1002/joc.3370100202.
- Marshall, B., and P. Plassmann, 2000: Mesh generation. *Handbook of Computational Geometry*, Elsevier, 291–332.
- Nešpor, V., 1995: Investigation of wind-induced error of precipitation measurements using a three-dimensional numerical simulation. Ph.D. thesis, Swiss Federal Institute of Technology Zurich, 109 pp., doi:10.3929/ethz-a-001442604.
- , and B. Sevruk, 1999: Estimation of wind-induced error of rainfall gauge measurements using a numerical simulation. *J. Atmos. Oceanic Technol.*, **16**, 450–464, doi:10.1175/1520-0426(1999)016<0450:EOWIEO>2.0.CO;2.
- Nitu, R., and Coauthors, 2012: WMO intercomparison of instruments and methods for the measurement of solid precipitation and snow on the ground: Organization of the experiment. *Proc. WMO Tech. Conf. on Meteorological and Environmental Instruments and Methods of Observations*, Brussels, Belgium, World Meteorological Organization, 16–18.
- Rasmussen, R., and Coauthors, 2001: Weather Support to Deicing Decision Making (WSDDM): A winter weather nowcasting system. *Bull. Amer. Meteor. Soc.*, **82**, 579–595, doi:10.1175/1520-0477(2001)082<0579:WSTDDM>2.3.CO;2.
- , and Coauthors, 2012: How well are we measuring snow: The NOAA/FAA/NCAR winter precipitation test bed. *Bull. Amer. Meteor. Soc.*, **93**, 811–829, doi:10.1175/BAMS-D-11-00052.1.
- Robinson, A., 1968: The aerodynamic characteristics of rain gauges. M.S. thesis, Department of Civil Engineering, University of Southampton, 253 pp.
- , and J. Rodda, 1969: Rain, wind and the aerodynamic characteristics of rain gauges. *Meteor. Mag.*, **98**, 113–120.
- Sevruk, B., 1982: Methods of correction for systematic error in point precipitation measurement for operational use. Operational Hydrology Rep. 589, WMO, 91 pp.
- , J. A. Hertig, and R. Spiess, 1991: The effect of a precipitation gauge orifice rim on the wind field deformation as investigated in a wind tunnel. *Atmos. Environ.*, **25**, 1173–1179, doi:10.1016/0960-1686(91)90228-Y.
- Smith, C., 2009: The relationship between snowfall catch efficiency and wind speed for the Geonor T-200B precipitation gauge utilizing various wind shield configurations. *Proc. 77th Western Snow Conf.*, Canmore, AB, Canada, Western Snow Conference, 115–121. [Available online at <http://www.westernsnowconference.org/node/751>.]
- , J. Hoover, J. Kochendorfer, and R. Nitu, 2012: Specifications for the WMO-SPICE single alter shield configuration. WMO-SPICE Tech. Doc., WMO, 6 pp. [Available online at <https://www.wmo.int/pages/prog/www/IMOP/intercomparisons/SPICE/Docs/Specifications%20SPICE%20Single%20Alter%20JH.PDF>.]
- Spalding, D., 1961: A single formula for the law of the wall. *J. Appl. Mech.*, **28**, 455–458, doi:10.1115/1.3641728.
- Strangeways, I., 2004: Improving precipitation measurement. *Int. J. Climatol.*, **24**, 1443–1460, doi:10.1002/joc.1075.
- Thériault, J., R. Rasmussen, K. Ikeda, and S. Landolt, 2012: Dependence of snow gauge collection efficiency on snowflake characteristics. *J. Appl. Meteor. Climatol.*, **51**, 745–762, doi:10.1175/JAMC-D-11-0116.1.
- Wilcox, D. C., 2006: *Turbulence Modeling for CFD*. 3rd ed. DCW Industries, 522 pp.
- WMO, 2008: Guide to meteorological instruments and methods of observation. 7th ed., WMO 8, 716 pp. [Available online at [http://library.wmo.int/pmb\\_ged/wmo\\_8\\_en-2012.pdf](http://library.wmo.int/pmb_ged/wmo_8_en-2012.pdf).]
- Wolff, M., K. Isaksen, A. Petersen-Øverleir, K. Ødemark, T. Reitan, and R. Bækkan, 2015: Derivation of a new continuous adjustment function for correcting wind-induced loss of solid precipitation: Results of a Norwegian field study. *Hydrol. Earth Syst. Sci.*, **19**, 951–967, doi:10.5194/hess-19-951-2015.
- Yang, D., 2014: Double Fence Intercomparison Reference (DFIR) vs. Bush Gauge for true snowfall measurement. *J. Hydrol.*, **509**, 94–100, doi:10.1016/j.jhydrol.2013.08.052.
- , and Coauthors, 1999: Quantification of precipitation measurement discontinuity induced by wind shields on national gauges. *Water Resour. Res.*, **35**, 491–508, doi:10.1029/1998WR900042.

Copyright of Journal of Hydrometeorology is the property of American Meteorological Society and its content may not be copied or emailed to multiple sites or posted to a listserv without the copyright holder's express written permission. However, users may print, download, or email articles for individual use.